







# Characteristics and interpretation of the seismic signal of a field-scale landslide dam failure experiment


**YAN Yan**<sup>1, 2</sup>  <http://orcid.org/0000-0002-3797-834X>; e-mail: yanyanyale@foxmail.com

**CUI Peng**<sup>1, 3\*</sup>  <http://orcid.org/0000-0003-2663-301X>;  e-mail: pengcui@imde.ac.cn

**CHEN Su-chin**<sup>4</sup>  <http://orcid.org/0000-0003-4796-5435>; e-mail: sachen@nchu.edu.tw

**CHEN Xiao-qing**<sup>1, 3</sup>  <http://orcid.org/0000-0002-0177-0811>; e-mail: xqchen@imde.ac.cn

**CHEN Hua-yong**<sup>1</sup>  <http://orcid.org/0000-0003-4033-3339>; e-mail: hychen@imde.ac.cn

**CHIEN Yi-liang**<sup>4</sup>  <http://orcid.org/0000-0001-5046-9467>; e-mail: tooen315@gmail.com

\* Corresponding author

<sup>1</sup> Key Laboratory of Mountain Surface Process and Hazards/Institute of Mountain Hazards and Environment, Chinese Academy of Sciences, Chengdu 610041, China

<sup>2</sup> University of Chinese Academy of Sciences, Beijing 100049, China

<sup>3</sup> Center for Excellence in Tibetan Plateau Earth Sciences, Chinese Academy of Sciences, Beijing 100101, China

<sup>4</sup> Department of Soil and Water Conservation, National Chung Hsing University, Taichung 40227, Chinese Taipei

**Citation:** Yan Y, Cui P, Chen SC, et al. (2017) Characteristics and interpretation of the seismic signal of a field-scale landslide dam failure experiment. *Journal of Mountain Science* 14(2). DOI: 10.1007/s11629-016-4103-3

© Science Press and Institute of Mountain Hazards and Environment, CAS and Springer-Verlag Berlin Heidelberg 2017

**Abstract:** Outburst floods caused by breaches of landslide dams may cause serious damages and loss of lives in downstream areas; for this reason the study of the dynamic of the process is of particular interest for hazard and risk assessment. In this paper we report a field-scale landslide dam failure experiment conducted in Nantou County, in the central of Taiwan. The seismic signal generated during the dam failure was monitored using a broadband seismometer and the signal was used to study the dam failure process. We used the short-time Fourier transform (STFT) to obtain the time–frequency characteristics of the signal and analyzed the correlation between the power spectrum density (PSD) of the signal and the water level. The results indicate that the seismic signal generated during the process consisted of three components: a low-frequency band (0–1.5 Hz), an

intermediate-frequency band (1.5–10 Hz) and a high-frequency band (10–45 Hz). We obtained the characteristics of each frequency band and the variations of the signal in various stages of the landslide dam failure process. We determined the cause for the signal changes in each frequency band and its relationship with the dam failure process. The PSD sediment flux estimation model was used to interpret the causes of variations in the signal energy before the dam failure and the clockwise hysteresis during the failure. Our results show that the seismic signal reflects the physical characteristics of the landslide dam failure process. The method and equipment used in this study may be used to monitor landslide dams and providing early warnings for dam failures.

**Keywords:** Landslide dam; Dam failure process; Field-scale experiment; Seismic signal

**Received:** 2 June 2016

**Revised:** 8 September 2016

**Accepted:** 20 October 2016

## Introduction

A landslide dam is a geological phenomenon common in mountainous areas. Such dams are formed following the blockage of a river channel by landslides or collapses. Landslide dams have a high probability of collapsing, leading to floods that can cause serious damage downstream (Sassa et al. 2005; Schuster 2006; Cui et al. 2009, 2013). Costa et al. (1988) investigated the outburst of 73 landslide dams and found that the main failure mode was overtopping, while the outbursts caused by piping and slope failure accounted for only a small proportion of the total. During overtopping processes, the breach in the longitudinal way developed in the means of head cut erosion, while in the cross way through the soil mass collapse. Overtopping outburst was a kind of erosion failure (Robinson et al. 1994; Temple et al. 1997; Hanson et al. 1997, 2001). To avoid or mitigate secondary disasters from landslide dam outburst floods, in-depth research on the characteristics of the breaching process of landslide dams is important. Advances in electronic technology has enabled the development of broadband seismic recording technology that can continuously record ground vibrations within the frequency range of 0–200 Hz and is able to detect even very weak signals. Broadband seismometers have distinct advantages of monitoring ground motion compared with accelerometers. Seismic signals recorded by broadband seismometers have been used in studies of natural hazards (e.g., avalanches, debris flows, and landslides) as well as in conventional earthquake research. Burtin et al. (2008) analyzed the spatiotemporal evolution of debris flows in the Himalayan region using high-frequency-band seismic signals and found that seismic signal analysis could be used to study mountain landslides and debris flows over relatively large areas. Huang et al. (2007) demonstrated that the impacts of bedload caused by debris flows were a major seismic source. Schmandt et al. (2013) analyzed the seismic signal of a controlled flood in the Grand Canyon (Colorado, USA) and found that the bedload, fluid, and fluid–air interface each had different frequency ranges. Seismic signals of different types of seismic sources (e.g., water flows, landslides, debris flows, and sediment) have distinct characteristics. While the signal caused by

debris flows is in the range of 10–150 Hz (Huang et al. 2007, 2008), the frequency of the signal generated by landslides is between 0.5 and 1.5 Hz (Feng 2011), vibration induced by the flow of water has a frequency of less than 10 Hz (Chao et al. 2015), and sediment-induced signals are mostly in the frequency range of 10–65 Hz (Schmandt et al. 2013). Thus, the characteristics of different events can be derived by analyzing the signal waveforms recorded by broadband seismometers (Deparis et al. 2008; Burtin et al. 2009; Hsu et al. 2011; Yamada et al. 2013). Relatively few studies have used seismic signals to investigate the landslide dam failure process and mechanism. Previous studies show that the signature of the surge wave caused by a dam breach has a trapezoidal shape and the stream water level and discharge rate are closely related to the frequency of the seismic signals (Feng 2012). To gain a deeper understanding of the characteristics of the landslide dam failure process, seismic signals generated during the failure process should be further investigated.

In this study, a field-scale landslide dam failure experiment was conducted in the Huisun Forest Area in Nantou County. The characteristics of the seismic signal recorded during the landslide dam failure process were investigated using the hydrodynamic parameters and soil mechanical parameters of the dam. We analyzed the variations in the seismic signal and determined the cause of the changes of the signal during the breaching process.

## 1 Experiment Setup

The study site is located in the downstream reaches of the Landao Creek Basin (Figure 1) in the northwestern end of the Huisun Forest Area in Nantou County. Landao Creek is a developing debris flow gully. For the purpose of our experiment, a sand discharge channel was constructed in the upstream reaches of Landao Creek. The inflow from the upstream area was controlled by adjusting the valve located between the reservoir and the sand discharge channel (Chen et al. 2015). Large amounts of debris flow deposits provided ample dam material for the experiment. Because of its characteristics, the Landao Creek site provides ideal experimental conditions.

Two field-scale landslide dams were constructed in the gully to facilitate the simulation of the dam failure process (Figure 1). The distance between the centerlines of the two dams was 64.8 m. The height and width of the upstream and downstream dams were 28.8 m, 3.0 m and 25.9 m, 3.0 m respectively. Both dams were constructed by piling soil at its natural angle of repose. A breach channel, approximately 2 m wide, was dug in the middle of each dam. Figure 1 shows the layout of the sensors.

The experiment was conducted on May 22, 2015. The main event was recorded between 11:00:00 and 11:58:00 (duration 3480 s). The videos recorded by digital video cameras and time-lapse cameras allowed us to determine the time of each event. In this experiment, we installed three sets of broadband seismograph. One was installed by us between the upstream and downstream dam

on the bank, to provide us with the experimental data. Others were installed by the University of Taiwan, only to provide data to correction. We built a cement base on the concrete pier on the bank, where the base and the bedrock were in full contact. We installed the broadband seismograph on the pedestal. The seismograph of Taiwan University was installed on the downstream bank of the downstream dam. They were installed under the ground 0.5 meters on the bedrock. The broadband seismometer obtained a three-component seismic signal at 0–50 Hz. We installed four water-level loggers in the impoundment areas of the upstream and downstream dams to acquire the water-level data. The outflow velocities of the landslide dams were measured using a self-developed trace projection transformation (TPT) method (Yan et al. 2016). Based on the water level data and the 3D models of the upstream and downstream dams, we

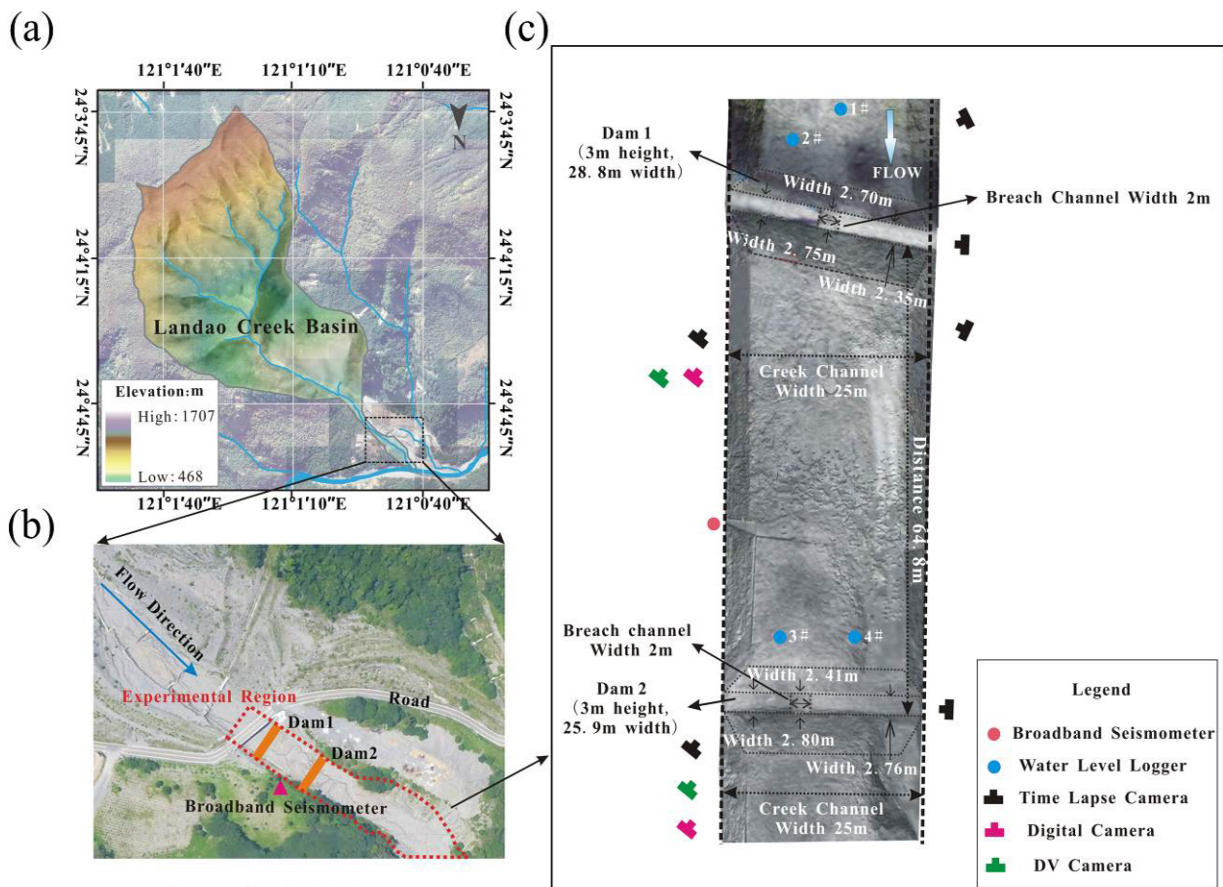


**Figure 1** Images showing the general conditions at the experiment area. (a) Location of Landao Creek Basin, Nantou County. (b) Aerial photo of the experiment site showing the two dams and seismometer location. (c) Experiment layout and dimensions.

calculated the changes in the capacities of the upstream and downstream lakes.

## 2 Methodology

### 2.1 Short-time Fourier transform (STFT) algorithm

Data analysis was performed to determine the changes in various frequency components with time. We performed a time–frequency domain transform of the seismic signal using STFT. To obtain a discrete time series ( $x[n]$ ), a time–frequency localized window function ( $\omega[n]$ ) was selected. The analysis window function  $\omega[n]$  is assumed stationary over a relatively short period. By moving the window function, we ensure that  $x[n]\omega[n]$  is a stationary signal within the applied finite time widths; hence, the power spectra of the signal at different moments can be calculated by Eq. (1).

$$STFT\{x(t)\}(m, \omega) = X(m, \omega) = \sum_{n=-\infty}^{\infty} x[n]\omega[n-m]e^{-j\omega n} \quad (1)$$

For the STFT process, a Hanning window with a length of 128 points was selected as the window function (Eq. (2)) because of its relatively wide analysis bandwidth and relatively small energy leakage.

$$\omega[n] = \begin{cases} 0.5 - 0.5 \cos\left(\frac{2\pi n}{N-1}\right), & (0 \leq n \leq N-1) \\ 0, & (others) \end{cases} \quad (2)$$

### 2.2 Power spectrum density (PSD)

PSD allows us to determine the signal power distribution at each moment, from which the characteristics and the source of each signal component can be derived. The PSD of the seismic signal in the frequency domain is defined as:

$$PSD_{f_{\min} \sim f_{\max}}(t) = \frac{1}{(f_{\max} - f_{\min})} \times \sum_{f=f_{\min}}^{f_{\max}} S(t, f) df \quad (3)$$

where,  $f_{\min}$  and  $f_{\max}$  represent minimum and maximum frequencies of the frequency band to be analyzed;  $t$  represents time, and  $S(t, f)$  represents the time–frequency power spectrum of the signal calculated using the STFT method.

### 2.3 Short-term-average/Long-term-average (STA/LTA) algorithm

In the dam failure scenario, sliding rocks struck the dams and the channel and generated a seismic signal, which was used to quantify the dynamic rockslide process. The seismic signal envelope of the rockslide was extracted using the STA/LTA method (Dammeier et al. 2011; Chen et al. 2013). During the processing, both the STA and the LTA of the seismic signal envelope were obtained using short duration ( $t_s$ ) and long duration ( $t_L$ ) time windows, respectively. The start time of the rockslide ( $T_1$ ) was set as the time at which the STA/LTA ratio exceeded the set value ( $\rho$ ), and the corresponding seismic amplitude was defined as  $A_1$ . The peak value of the seismic signal envelope is defined as the peak ground velocity (PGV); the seismic amplitude decreased after the PGV was reached. The end of the rockslide event was defined as the time ( $T_2$ ) at which the seismic amplitude decreased to the proportion  $p$  of the PGV energy, and its corresponding amplitude was  $A_2$ . The duration of the sliding rock event is  $DUR = T_2 - T_1$ . Because the envelope area ( $A_E$ ) of the rockslide is related to the total energy released by the sliding rocks (Dammeier et al. 2011), the envelope area can be calculated using Eq. (4).

$$A_E = \int_{T_1}^{T_2} (E(t) - E_0) dt \quad (4)$$

where,  $E(t)$  represents the root mean square amplitude at time  $t$  and  $E_0 = (A_1 + A_2) / 2$  represents the noise level. By analyzing the rockslide signal response, the frequency and scale of each rockslide event can be obtained.

## 3 Results and analysis

The experiment began at 11:00:00 and terminated at 11:58:00. For the analysis we extracted the data recorded from the time when the inflow arrived at the upstream dam (11:29:23) to the time the outburst flood of the downstream dam stabilized (11:56:32) (duration 1629 s). The video footage acquired shows the various stages of the experiment, including the failure of two dams. Table 1 summarizes the main features observed in each stage of the experiment. The water–sediment data includes the water level, outflow velocity,



discharge rate, and breach width. To examine the various stages of the process, we treated the upstream impoundment stage (A-B) as one entity, the stage prior to dam failure. We also treated the upstream dam overtopping stage (B-C), the upstream dam failure stage (C-D), the downstream dam overtopping stage (D-E), and the downstream dam failure stage (E-F) as another entity in the

dam failure stage. The steady stage after dam failure (after F) was treated as a third individual entity (Table 2).

The broadband seismometer recorded the seismic signals in three directions (east, north, and vertical). The time-series (Figure 2) of the seismic signals in the three directions exhibit similar patterns. The signal amplitude gradually decreased

**Table 1** Observed characteristics of each stage of the landslide dam failure process

Upstream event	Occurrence time	Downstream event	Occurrence time
Impoundment started in the upstream area	1763 s	The upstream outburst flood flowed downstream	2729 s
The upstream dam loosened, and gradually subsided	2625 s	The downstream flood overtopped the dam	2814 s
The upstream dam started collapsing from its middle section	2674 s	The downstream dam collapsed at a large scale	2934 s
The upstream dam outburst at a large scale	2756 s	The velocity of the downstream flood stabilized	3160 s
Upstream rocks slid	2680 & 2980 s	Downstream rock slid	3083 s
The velocity of the upstream flood stabilized	3139 s		

**Table 2** Characteristics of each stage of the landslide dam failure process

Stage	Event	Occurrence time
A-B: Stage prior to dam failure B-C-D-E-F: Dam failure stage F-: Steady stage following dam failure	A: Water arriving at upstream 1# Dam	1763 s
	B: Overtopping of upstream 1# Dam	2674 s
	C: Failure of upstream 1# Dam	2756 s
	D: Overtopping of downstream 2# Dam	2814 s
	E: Failure of downstream 2# Dam	2856 s
	F: Stable condition following failure	3160 s

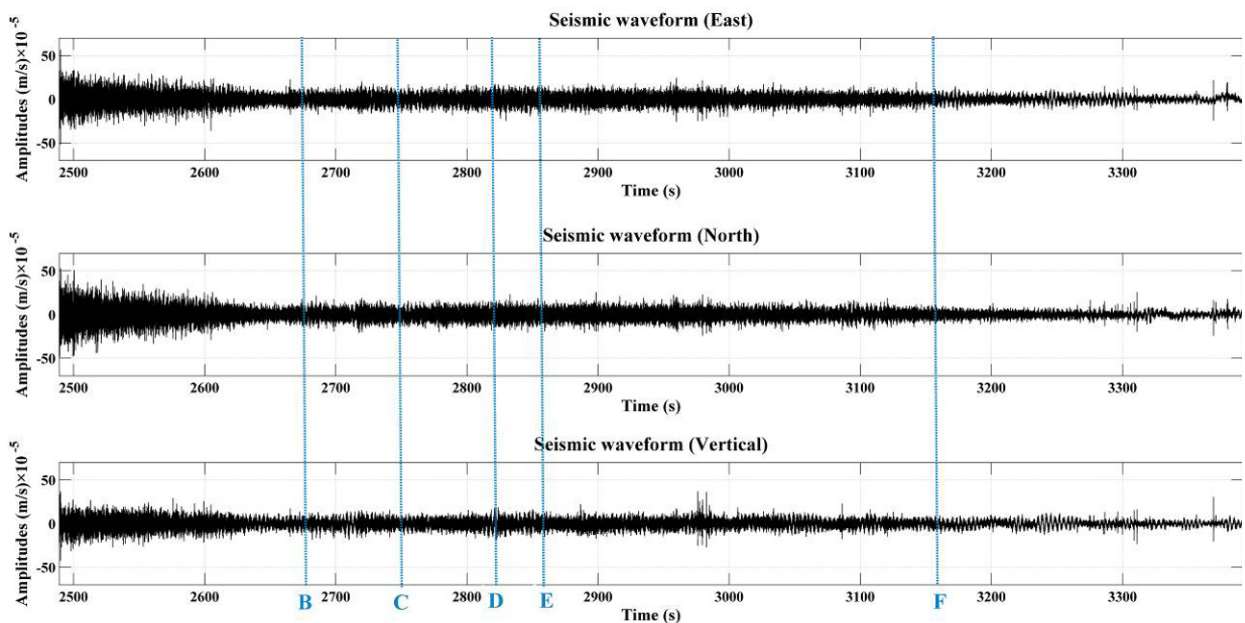


**Figure 2** Time-series of the seismic signals recorded by the broadband seismometer in the east, north, and vertical directions.

from  $t = 2488$  s to 2674 s, followed by strengthening and weakening in between 2674 to 3160 s.

### 3.1 Time–frequency characteristics of the seismic signal

Because the dominant seismic signal generated by soil collapse and rockslides is the vertical seismic component (Burtin et al. 2008, 2009; Roth et al. 2014) and the seismic signals from the three directions had similar temporal distributions (Figure 2), we selected the vertical seismic signal for the time–frequency analysis. We performed STFT on the time-series of the vertical component of the signal; the frequency spectra for the period 2488–3392 s is shown in Figure 3. The spectra can be divided into three main bands: a low-frequency band (0–1.5 Hz), an intermediate-frequency band (1.5–10 Hz), and a high-frequency band (10–45 Hz). The energy generated in this experiment was mainly concentrated in the 10–45 Hz frequency band (the high-frequency band). The energy decreased from 2488 to 2674 s, slowly increased from 2675 to 3160 s, and then stabilized, with a subsequent decrease from 3161 to 3288 s. In the intermediate-frequency band, a number of short-term signals appeared at 2682 s, 2982 s, and 3084 s. In the low-frequency band, most of the energy was concentrated in the periods 2708–2722 s, 2804–2851 s, and 2877–2947 s.

#### 3.1.1 Stage prior to dam failure

During the stage prior to the dam failure (Figure 4), the signal amplitude increased gradually at first, peaking at approximately 2425 s, and then decreased. After 2475 s, the amplitude became steady. The main energy band was concentrated at 20–35 Hz. The energy concentration shifted towards the higher frequency, reaching the maximum energy level recorded during the experiment. The time–frequency spectra of the signal shows that the frequency of the main energy signal before 2500 s was well defined and the component beyond the main energy frequency attenuated rapidly. After 2500 s, the spectra dispersed, with the frequencies distributed within the band 10–40 Hz. After  $t = 2550$  s, the spectra dispersed further, and the energy shifted toward the lower frequencies.

#### 3.1.2 Dam failure stage

During the dam failure stage, the signal amplitude did not vary much and no significant anomalous amplitudes appeared. The amplitude was smaller than that prior to the dam failure; it was generally higher at first and then decreased. The evolution of the spectra with time (Figure 5) shows that the main energy shifted toward the lower frequencies, primarily 20–30 Hz. The energy level was about one fifth of that prior to the dam failure. The energy was relatively high at the low

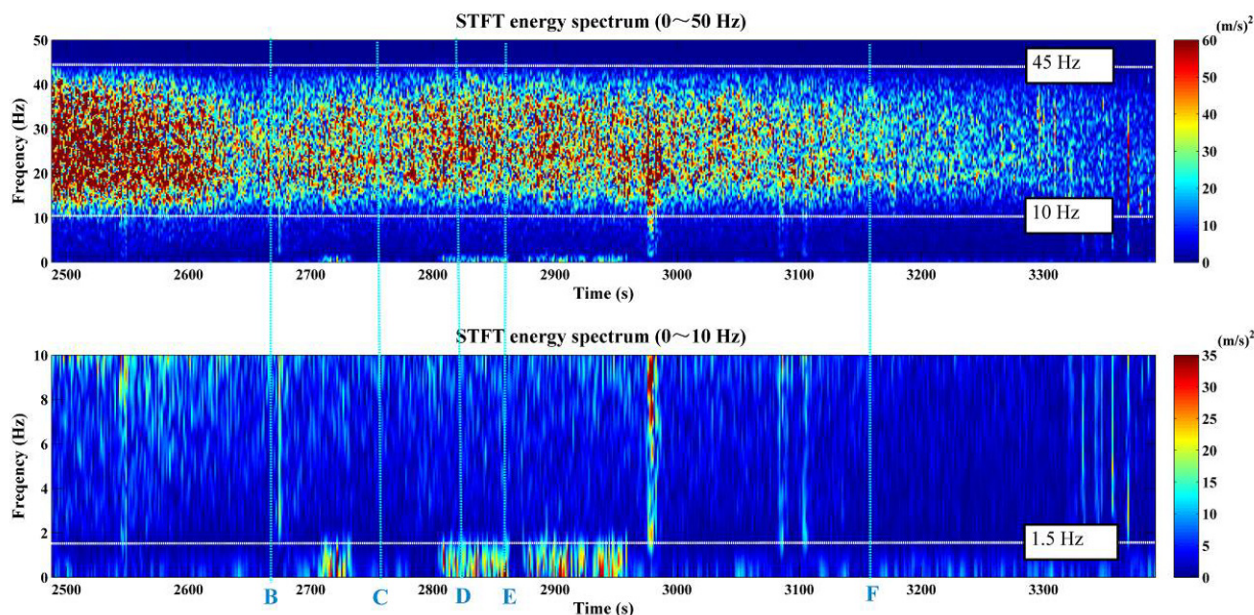
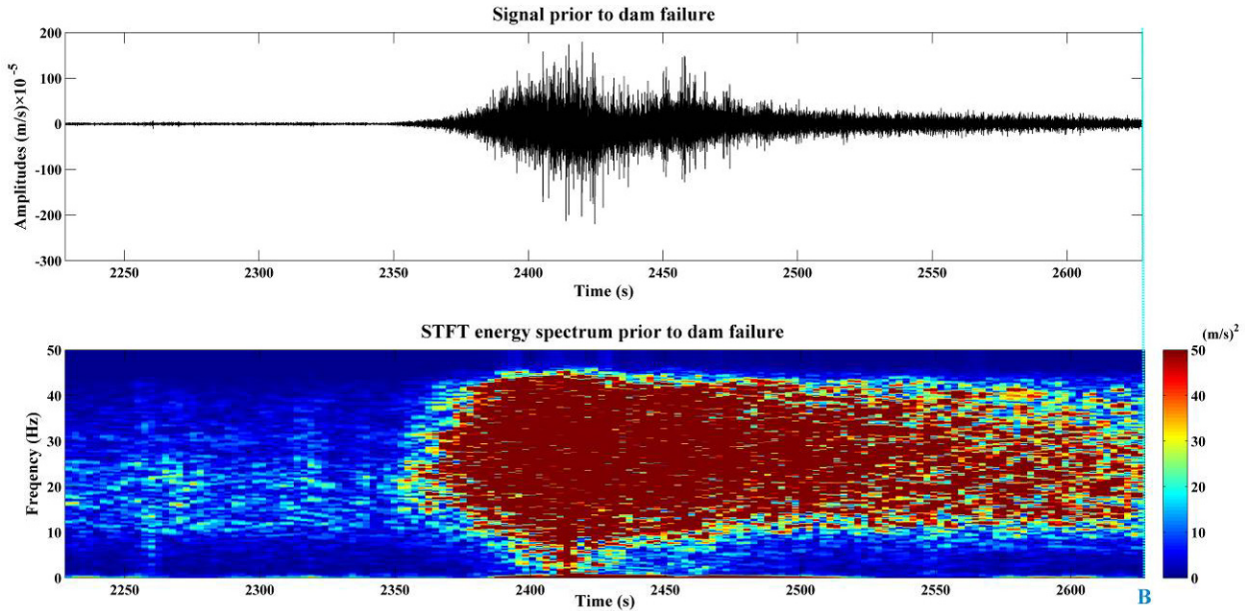


Figure 3 STFT time–frequency spectra of the vertical seismic signal.



frequency band (approximately 15 Hz), with small variations in the amplitude at 15–30 Hz and stable signal spectra. The level of the low-frequency energy increased rapidly, whereas that of the high-frequency band decreased slowly. The time–

frequency spectra did not show a clear pattern with time; the frequency band of the main energy changed from 10–30 Hz to 10–40 Hz and then back to 10–30 Hz. The variation in the main energy frequency indicates an event that led to an increase



**Figure 4** Seismic signal and time–frequency spectra before the dam failed.

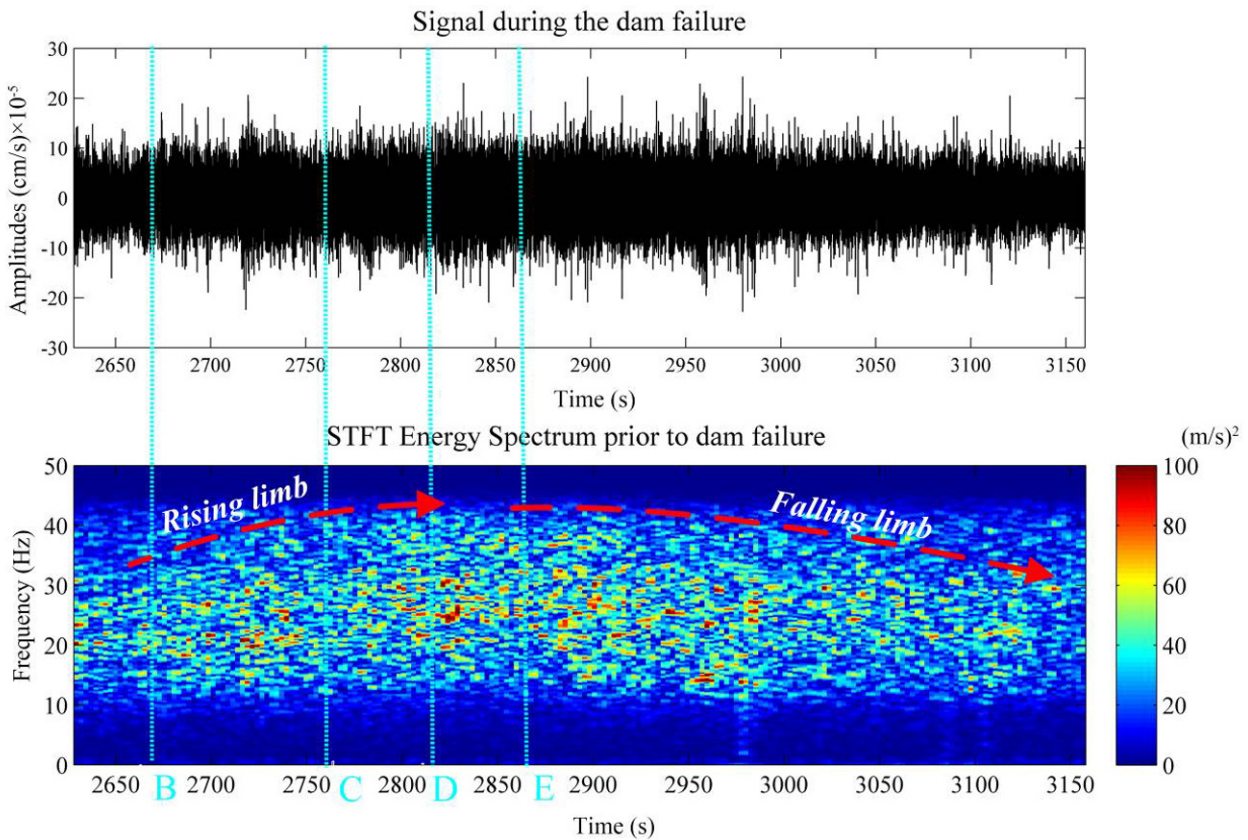


**Figure 5** Seismic signal and time–frequency spectra during the dam failure stage.

in the high-frequency component.

### 3.1.3 Steady stage following dam failure

During the steady stage after the dam failure, the energy level was much lower than during the two earlier stages. The frequency spectra did not show a well-defined pattern with time; most of the energy was distributed within a narrow frequency band, and the corresponding energy was very low (Figure 6). The energy level showed a decreasing trend with time, and the entire system became stable. In the last stage, the seismic signal was generated only by the water flow. The data corresponding to this stage can be used to study the characteristics of the single seismic signal generated by water flow.

### 3.2 Correlation of the PSD and water level

PSD analysis of the signal can provide us with the distribution of the signal power at each frequency, which helps to analyze the variations of frequency and energy. Meanwhile, the water flow parameters, particularly the water level, have a significant effect on the dam failure process. Changes in the water level can cause erosion and the collapse of the dam, and dam erosion and collapse will also result in water-level changes.

Thus, by analyzing the correlation of the water level and PSD, we can gain a deeper understanding of the process of landslide dam failure.

To investigate the relationship between the PSD and water level and the effects of water-level variations on each frequency band, we analyzed the PSD and water level at different frequency bands. STFT data was extracted from three frequency bands (0–1.5 Hz, 1.5–10 Hz, and 10–45 Hz), the energy of each frequency band was divided by the frequency width, and each stage was divided into 25 groups with duration of 20 s and overlaps of 10 s between two consecutive groups. We then calculated the PSD of each frequency band. By treating the water level as the independent variable and the PSD as the dependent variable, we obtained the relationship between the water level and PSD. In Figures 7–9, the color of the data points indicates the time sequence of the sampling points. The color gradually shifts from blue at the initial sampling point to orange at the last sampling point.

#### 3.2.1 Stage prior to dam failure

The variation of the PSD of each frequency band as the water level increased before the dam failure can be divided into three segments (Figure 7): (1) when the water level <1 m, the variation in

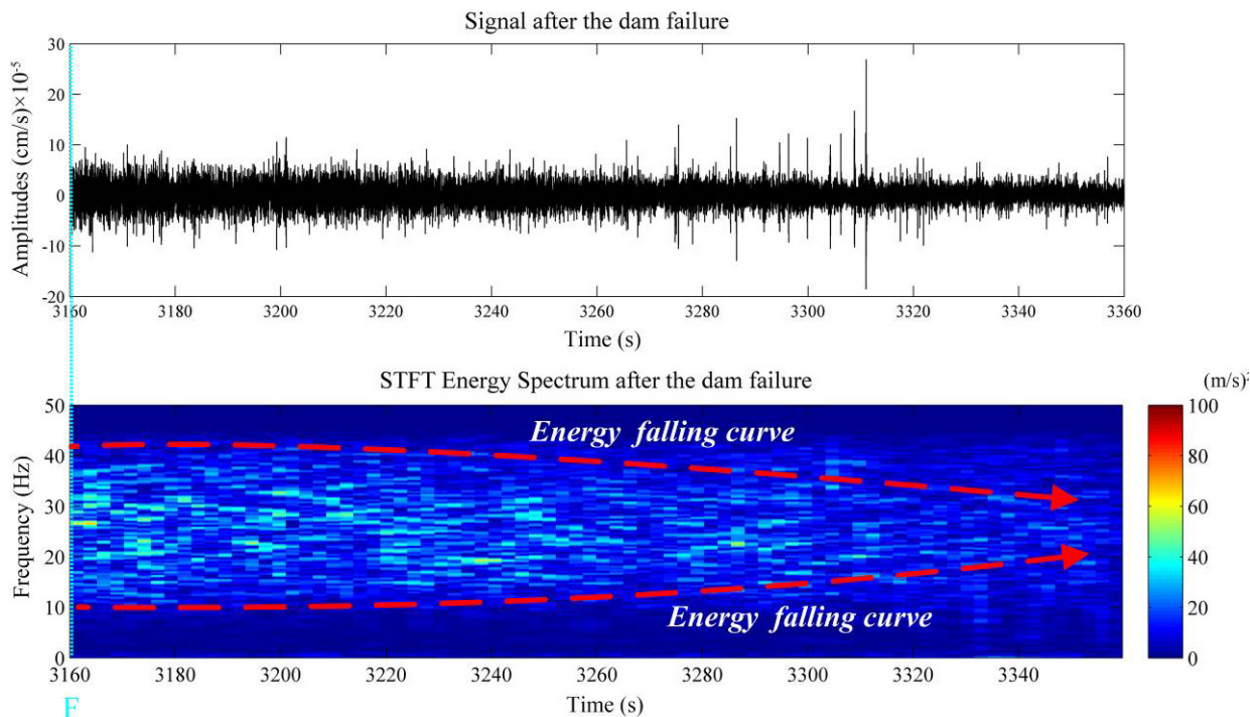


Figure 6 The signal and time–frequency spectra of the steady stage.



the PSD was very less as the water level raised; (2) as the water level rose from 1 to 1.2 m, the PSD rapidly increased; (3) with further raise in water level, the PSD decreased. The trends of the PSDs associated with the various frequency bands differed. In the frequency bands 0–1.5 Hz and 1.5–10 Hz, after the water level exceeded 1.2 m, the PSDs first decreased and then increased.

### 3.2.2 Dam failure stage

The PSD variation with increasing water levels during the dam failure stage can be divided into two segments: an early segment in which the PSD increased with rising water levels and a later segment in which the PSD decreased with falling water levels (Figure 8). The low-frequency and high-frequency bands differed. The rising and falling segments of the low-frequency band (0–1.5 Hz) intersect a few times, while those at 1.5–10 Hz intersect only twice. At 10–45 Hz the two segments are at different levels, indicating increasing PSD levels with rising water levels and decreasing PSD levels with falling water levels, showing clear rising

and falling limbs which result in significant clockwise hysteresis flow.

### 3.2.3 Steady stage following dam failure

Unlike the PSD plots of the first two stages, the PSD plots of the three frequency bands in the steady stage following dam failure exhibit a random distribution (Figure 9). Overall, the PSD decreased with rising water levels.

## 3.3 Variations in the signal during the dam failure experiment

To examine the causes of the variation in the seismic signals recorded during the dam failure experiment, we first looked at the seismic signal in the three frequency bands and the corresponding video footage.

### 3.3.1 Variations in the seismic signal at each frequency band

#### 3.3.1.1 Low-frequency band

Figure 10 shows the frequency power spectra

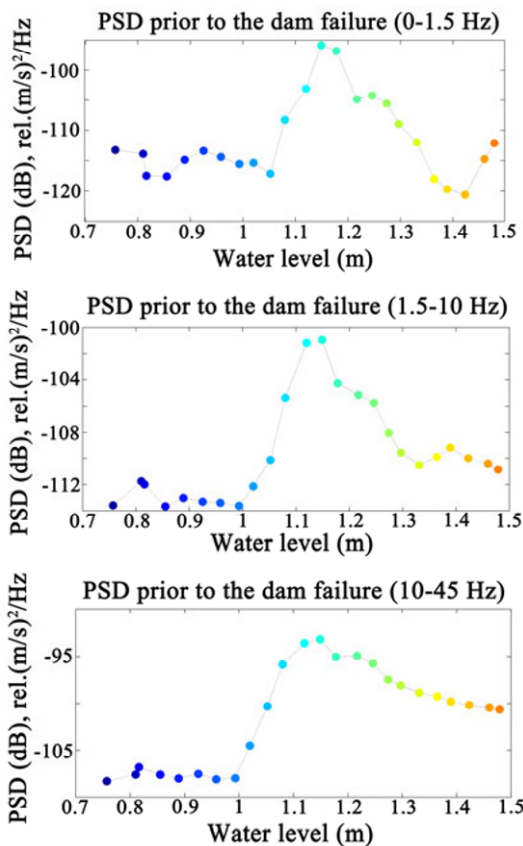


Figure 7 Scatter plots of the power spectral density of each frequency band versus water level before dam failure.

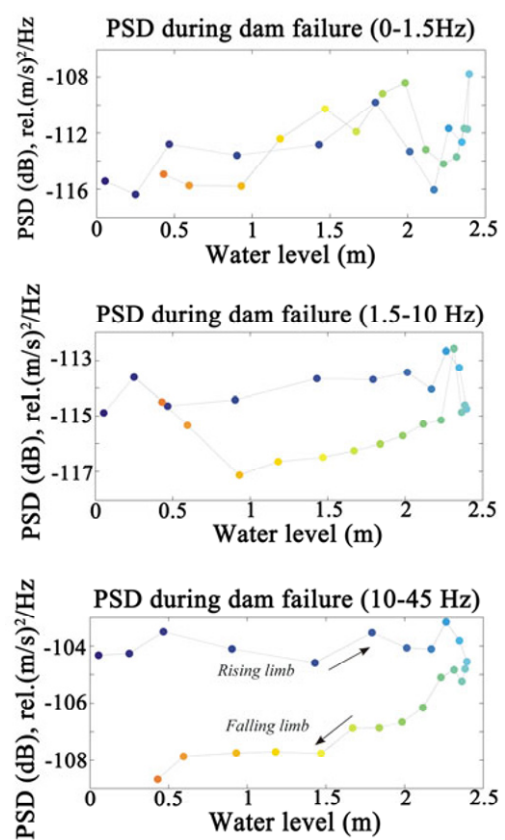
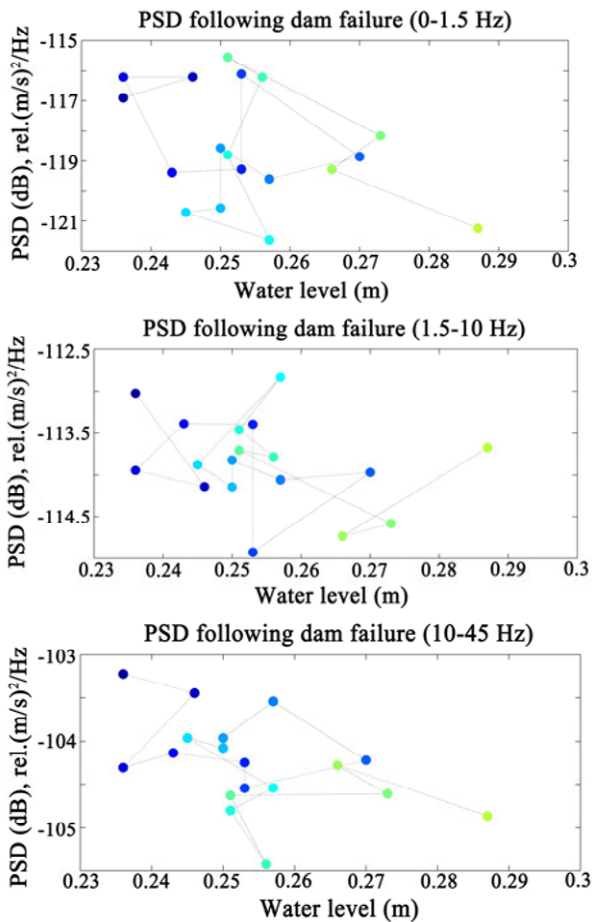


Figure 8 Scatter plots of the power spectral density of each frequency band versus water levels during dam failure.

during the experiment. The periods covering the upstream and downstream dam collapse events, recorded on video, correspond to the blue box (2674–2864 s) and green box (2814–2963 s),



**Figure 9** Scatter plot of the power spectral density of each frequency band versus water levels during the steady stage following dam failure.

respectively. The energy level of the low-frequency-band component was significantly higher during these two periods than during the stable periods. In addition, multiple relatively large-scale dam collapse events occurred at the upstream dam breach, and large pieces of soil detached from the dam and slid down to the riverbed during the periods 2708–2722 s and 2804–2851 s. Multiple relatively large-scale dam collapse events occurred at the downstream dam breach during the period 2851–2947 s. The seismic energy levels during these collapse events were higher than during the stable state and correspond to the low-frequency-band seismic signals as shown in Figure 3. Good agreement was found between the timing and duration of the power spectra peaks (Figure 10) and those of the high-amplitude signals on the time–frequency analysis (Figure 3) as well as with the video images of the dam collapse events and their scale (Table 3). This demonstrates that the low-frequency band (0–1.5 Hz) component of the seismic signal was caused by the soil collapse in the dams during the dam failure process.

### 3.3.1.2 Intermediate-frequency band

Three main rockslide events were observed in the video footage. Rock slides #1 and #2 represent events in which rocks slid down from the upstream dam and struck the riverbed, while in rock slide #3 the rocks slid down from the downstream dam and struck the riverbed. The timing and duration of the high-amplitude peaks in Figure 3 and the high-energy peaks in the medium-frequency power spectra (Figure 11) are in good agreement with the three recorded rock-slide events, indicating that

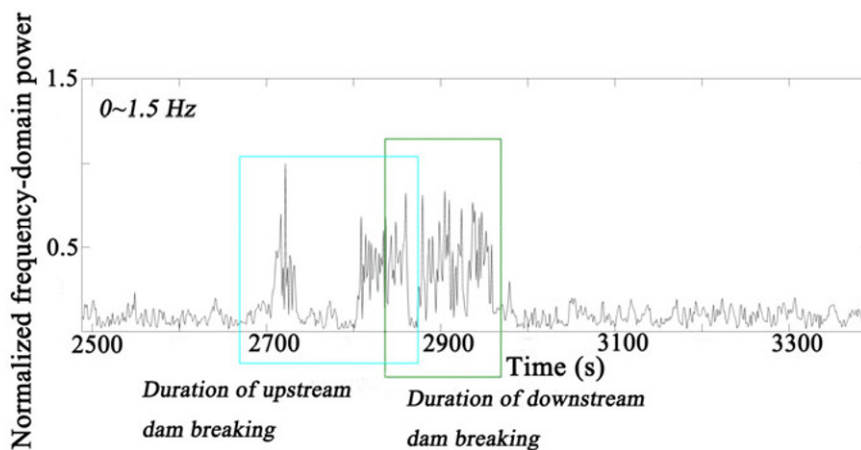


**Figure 10** Time–energy changes in the low-frequency band (0–1.5 Hz) of the vertical seismic signal.

**Table 3** Soil collapse events in the upstream and downstream dam during the dam failure experiment

Event time	Location	Breach width	Event time	Location	Breach width
2708–2722 s	Upstream	0.0–0.3 m	2895–2898 s	Downstream	5.7–6.6 m
2804–2851 s	Upstream	2.5–6.3 m	2903–2908 s	Downstream	7.0–7.9 m
2850–2854 s	Downstream	3.9–4.0 m	2918–2920 s	Downstream	8.1–8.6 m
2857–2862 s	Downstream	4.0–5.1 m	2921–2925 s	Downstream	8.6–9.0 m
2877–2881 s	Downstream	5.1–5.3 m	2935–2938 s	Downstream	9.8–10.7 m
2888–2892 s	Downstream	5.3–5.7 m	2943–2947 s	Downstream	10.8–11.4 m

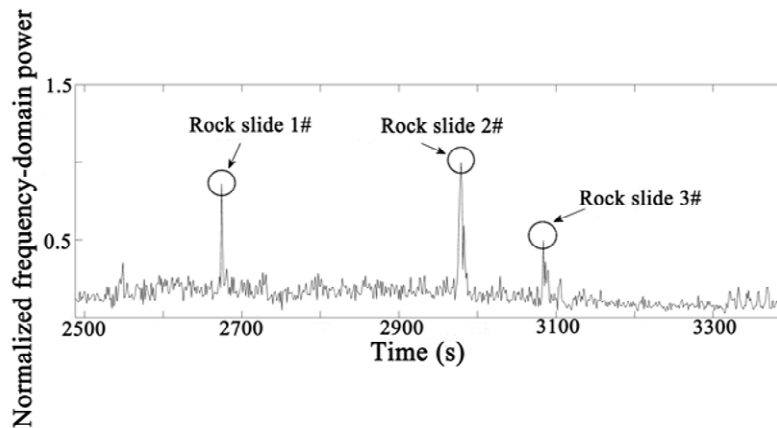


**Figure 11** Time–energy changes in the intermediate-frequency band (1.5–10 Hz) of the vertical seismic signal.

the high-energy events observed in the 1.5–10 Hz signals represent rock slides.

The seismic signal can be used to analyze the rockslide process dynamically. The method for analyzing the dynamic rockslide process presented in section 3 identified several relatively intense signal peaks before the arrival of the rockslide signal. These peaks may represent relatively weak collision events and other noise. During the data processing, we eliminated these peaks and then averaged the data using a short-duration time window of 0.05 s and a long-duration time window of 1 s. The time at which the STA/LTA ratio exceeded 3 was used as the start time of the rockslide ( $T_1$ ), and the corresponding seismic amplitude was  $A_1$ . The end time of the rockslide was defined as the time at which the seismic amplitude decreased to 10% of the PGV energy, and the corresponding seismic amplitude was  $A_2$ . Accordingly, the durations (DUR) of rockslides #1–#3 were 2.5, 2.9, and 2.1 s, respectively (Figure 12). Using the video recordings of the rockslides, we established the path lengths ( $D_{fall}$ ) of the three rockslides as 4.2, 3.6, and 3.8 m, respectively. Thus, the average rockslide velocities were 1.68, 1.24, and 1.81 m/s, respectively. The envelope areas ( $A_E$ ) of the seismic signal released by the three rock slides

were calculated using Eq. (4), which are 794.18, 1240.70, and 338.90  $m \times 10^{-5}$  (Table 4) respectively, to obtain the scales of the rockslides during the landslide dam failures.

### 3.3.1.3 High-frequency band

Previous studies on the frequency of water flows and sediment movement found that the frequency of the signal generated by water flow was less than 10 Hz and the frequency of the signal generated by sediment movement was 10–65 Hz (Schmandt et al. 2013; Roth et al. 2014; Chao et al. 2015). The spectral analysis of the signal generated in our experiment indicated that most of the seismic signals (Figure 3) were within the frequency range of 10–45 Hz, which was interpreted as seismic waves generated by sediment movement.

During the period 2488–2674 s, the inflow was impounded against the upstream dam. The water flowed rapidly along the riverbed, which resulted in relatively intense movement of the sediment; hence, the high-frequency component (10–45 Hz) of the seismic signal had relatively high energy during this period (Figure 3). The inflow accumulated behind the upstream dam; thus, it was buffered by the impounded water, leading to



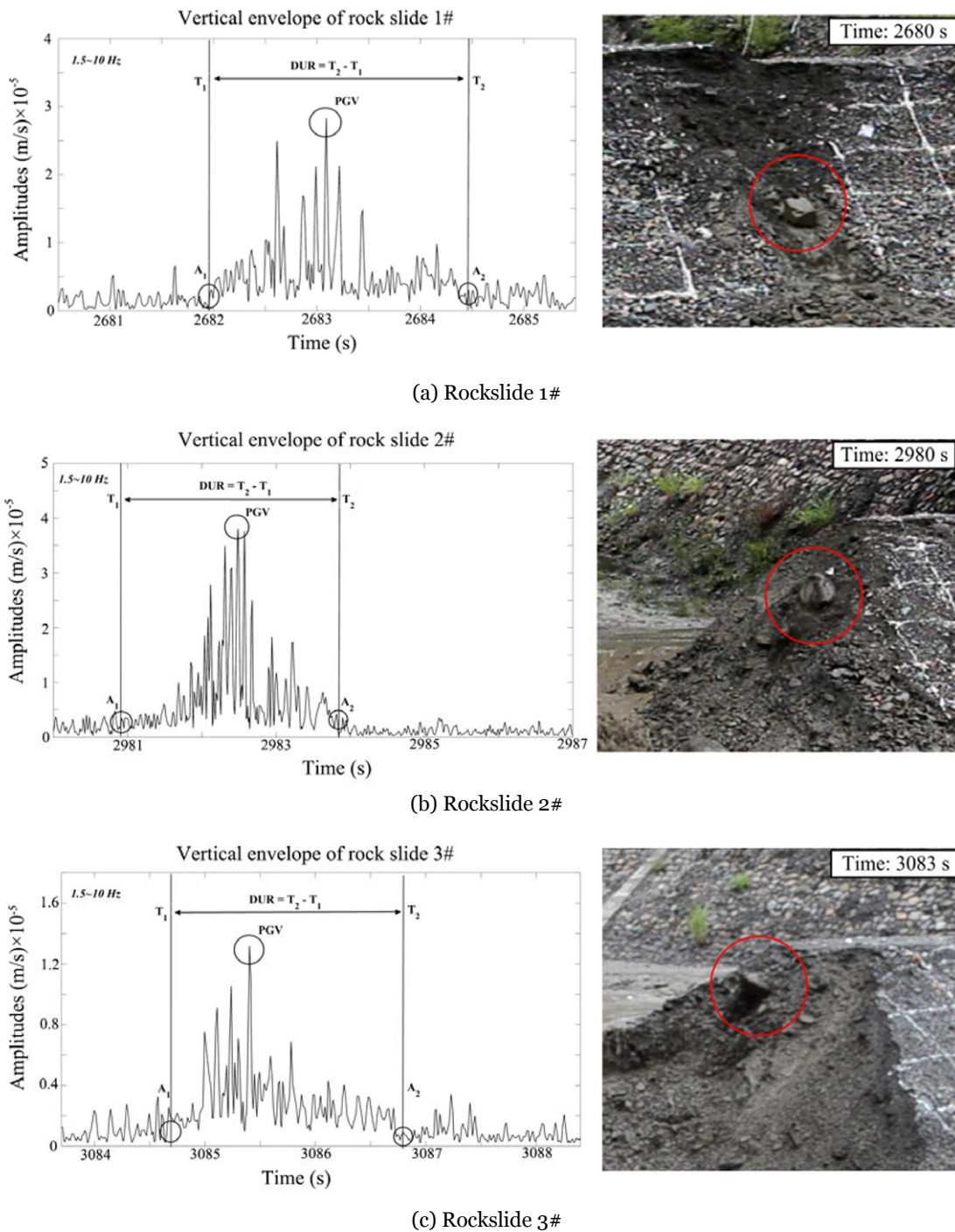


**Figure 12** Seismic signal envelope (left) and image (right) of the three rock slides in the dam failure experiment.

**Table 4** Calculated parameters of the three rock slide events

Event	Occurrence time (s)	$D_{fall}$ (m)	$DUR$ (s)	$V_f$ (m/s)	$A_E$ (m) $\times 10^{-5}$
Rock slide 1#	2680	4.2	2.5	1.68	794.18
Rock slide 2#	2980	3.6	2.9	1.24	1240.7
Rock slide 3#	3083	3.8	2.1	1.81	338.9

**Notes:**  $D_{fall}$  is the path length by the video recordings of the rockslide; The duration of the sliding rock event is  $DUR = T_2 - T_1$ ;  $V_f$  is the average rockslide velocity; The envelope area ( $A_E$ ) of the seismic signal released by the rock slide is calculated using Eq.(4).

decreased flow velocity of the water, which resulted in less movement of the sediment and a decrease in the energy of the high-frequency component. Because of the continuous erosion by water during the previous period and by the water pressure, the eroded surface area of the upstream dam expanded and small-scale collapses started to occur. At 2674 s, the water overtopped the upstream dam and the dam started to collapse. At that time, the energy of the high-frequency component gradually increased. During 2674–2814 s, the volume of water flooding from the upstream dam to the downstream dam increased and continuously eroded the downstream dam. At 2814 s, the flood overtopped the wall of the downstream dam, and the outburst flood rapidly flowed downstream via the breach, which further eroded the breached wall and destabilized the dam. The outflow continued to increase until 3160 s. From the time when the upstream and downstream dams burst to the time when the flooding stabilized (2674–3160 s), the energy of the high-frequency component remained high. After 3160 s, because the movement of the sediment at the dam breaches gradually weakened, the energy of the high-frequency component decreased gradually. Thus, based on the energy level of the high-frequency component, the movement of sediment in the areas near the dam breaches can be determined.

### 3.3.2 Variations in the seismic signal before dam failure

The energy of the signal during the stage prior to dam failure varied significantly, i.e., a trend of initial increase followed by a decrease. The frequency band first widened and then narrowed (Figure 4). The PSDs initially increased and then decreased with water level variations (Figure 7). These trends were completely different from the typical clockwise hysteresis.

The PSD is mainly controlled by the sediment particle size ( $D$ ), particle quantity ( $n$ ), and movement velocity ( $w_i$ ) (Tsai et al. 2012):

$$P_v^T \approx \int_{t_i}^n \frac{\pi^2 f^3 m^2 w_i^2}{\rho_s^2 v_c^3 v_u^2} \chi(\beta) dD \quad (5)$$

The movement of the sediment is the main source of the seismic signal. Particle movement requires an external force exceeding a critical value. Figure 13a shows the configuration of the forces acting on a particle that has started to move from a

stationary state: the effective gravity ( $W$ ), horizontal force ( $P_x$ ), and vertical uplift force ( $P_y$ ). The horizontal force is mainly controlled by the water flow. The uplift force is created mainly by the pressure gradient caused by the velocity difference above and below the particle. Flow velocity varies when it flows around particles. As shown in Figure 13b, the denser arrow represents higher velocity. According to Bernoulli's equation (Eq. (6)), a particle in a moving fluid is subject to an upward pressure gradient.

$$\frac{P}{\rho} + gy + \frac{v^2}{2} = C \quad (6)$$

The pressure gradient is controlled mainly by the velocity of the fluid. In turbulence, there is also an eddy uplift force, which is also a main source of the vertical uplift force. When  $P_x$  and  $P_y$  can overcome the resistance due to  $W$  and friction, the particle starts to move in the form of sliding or rolling. When  $P_y$  is larger than  $W$ , the particle starts to move in the form of saltation. The velocity of saltation particles that collide with the riverbed exceeds the velocity of sliding and rolling. Eq.(5) shows that the particle velocity ( $w_i$ ) is positively correlated with the energy of the seismic signal. With further increase in  $P_y$ , the particle motion may change from saltation to suspension. Suspended particles mix with the water and

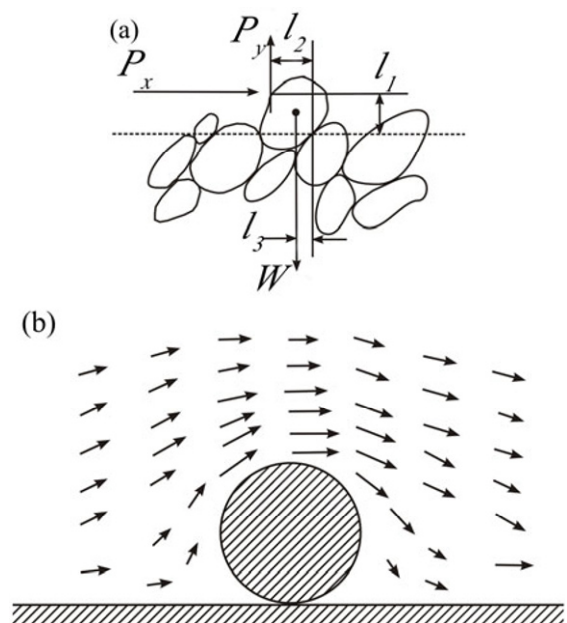


**Figure 13** (a) Forces acting on particles in the water flow. (b) Water flowing around a particle; denser streamlines denote higher velocity.

increase its density, thereby increasing the energy of the signal generated by the water flow.

In this experiment, the inflow was blocked in the channel behind the upstream dam. The inflow velocity decreased, and the inflow gradually pooled and formed a slow return flow behind the upstream dam. Because the reservoir behind the dam was shallow when the water initially arrived (before 2350 s), the velocity in the reservoir was very low. The pressure gradient generated by this condition was small (Eq. (6)), and the  $P_x$  generated by the water flow was also relatively small. With further rise in the water level, the force of the upstream flow and impoundment by the upstream dam created a return flow – an eddy with a relatively high velocity, which was much greater than the velocity of the inflow. This increased the quantity, particle size, and velocity ( $w_i$ ) of the particles carried by the water. The signal energy increased, and the frequency band widened simultaneously. When the signal energy started to increase, due to the rising water level behind the dam, the return flow velocity behind the dam increased rapidly and the uplift force generated by the eddy also increased rapidly, leading to a further increase in the frequency width. When the water of the reservoir reached a certain level where the velocity of the inflow was constant, its energy did not increase the return flow velocity further, and thus, the gradual increase in water volume decreased the velocity of the return flow. The decrease in velocity reduced the uplift and horizontal force, leading to a change in the frequency width from increasing to gradually decreasing. However, as the water flow increased, its capacity to carry particles continued to increase, and the signal energy thus displayed a trend of continuous increase. The return flow velocity gradually decreased with rising water levels. After the water reached a certain level, a layer of laminar flow formed at the bottom of the riverbed and eventually developed into a layer of slow return flow. At this time, the return flow behind the dam served as an energy buffer against the flow from upstream. The particle transport capacity of the return flow decreased and the frequency width of the seismic signal narrowed. Meanwhile, the energy also gradually decreased (Figure 4).

The variations in the energy and frequency of the seismic signal before the dam failure reflect a

dynamic process of inflow and return flow upstream of the dam in the water impounded by the upstream dam. The changes in the frequency width reflect the variation in water velocity, and the signal energy levels reflect the sediment transport capacity of the water.

### 3.3.3 The clockwise hysteresis during dam failure

Clockwise hysteresis in seismic signals generated by water and sediment flow has been observed and studied by many authors. There are various explanations for the energy and frequency of the corresponding seismic signals under different water conditions (Nanson 1974; Reid et al. 1985; Dietrich et al. 1989; Humphries et al. 2012; Martin and Jerolmack 2013; Roth et al. 2014). In this experiment, the hysteresis effect occurred mainly in the high-frequency band during the dam failure stage (Figure 8). This effect can be attributed mainly to the water flow in the channel between the two dams. The rising water level in this channel was governed by the failure of the upstream dam, which created a high-velocity flood between the upstream and downstream dams. The downstream dam failure caused another flood which was greater than the upstream flood, causing the water level between the two dams to fall.

When the upstream dam burst, flood water flowed downstream through the dam breach causing further erosion in the breach. As the outflow velocity increased, the frequency band of the signal widened, and its energy increased. The floodwater from the upstream dam pooled behind the downstream dam, forming a return flow and eddy similar to those that formed earlier behind the upstream dam. As the water level began to rise, the flood energy gradually increased, as shown in the scatter plot of the PSD versus water levels (Figure 8). The PSD increased slightly; this may be caused by a very small increase in the return flow velocity above the downstream dam caused by the flood from upstream. With the continuous water level rise between the two dams, the water flow from upstream gradually decreased, causing a decrease in the flow velocity and sediment transport capacity. Thus, the signal spectrum shows a decrease in the energy of the high-frequency component (Figure 5) and the PSD energy of the high-frequency band decreased with



the rising water level (Figure 8).

Following the failure of the downstream dam, the water flowed through the dam, causing the water level to fall after its earlier rise. During this period of downstream dam outburst, the water did not develop a return flow; rather, it flowed directly downstream. The sediment transport was completely controlled by the outburst flood. The maximum flow velocities at the failure of the upstream and downstream dams were similar, but the velocity of the upstream dam flow decreased at a faster rate than that of the downstream dam, until the two dam velocities finally stabilized. Before the water level stabilized, the discharge from the downstream dam exceeded the inflow from the upstream dam; therefore, its velocity was larger than the flood velocity from the upstream dam at a given water level. Due to the lack of return flow, the interactions between the moving sediment and the riverbed decreased and weakened. Thus, as shown in the scatter plot of the PSD versus water levels (Figure 8), at a given water level, the PSD with falling water levels was less than that with rising water levels.

In this experiment, the variation of the rising and falling segments of the water flow was the main reason for the formation of the clockwise hysteresis. The water formed a return flow when striking the dam and consequently formed an eddy. At a given water level, because the rising limb impacted the return flow while the falling limb did not, the energy of the rising limb exceeded that of the falling limb, resulting in the clockwise hysteresis.

#### 4 Discussion

The variations in the energy levels and frequency of the seismic signal generated by water and sediment during a dam failure event reflect the changes in the water flow and sediment movement in the water–sediment system. Thus, it is feasible to study the breaching process of a landslide dam based on the characteristics of the seismic signals recorded during the event. The correlation between the recorded seismic signals and video footage of the event indicate that the low-, medium-, and high-frequency bands can represent different events associated with the landslide dam failure. A

sudden increase in the low-frequency energy corresponds to a soil collapse event; an increase in intermediate-frequency signals corresponds to a rockslide event, while the high-frequency signals reflect the variations in the movement and quantity of sediment being transported by the water flow. These variations correspond to a series of events that constitute the entire landslide dam failure process. By analyzing the low-frequency, intermediate-frequency, and high-frequency bands of the seismic signal, we can develop a representation of the seismic signal corresponding to each event during the evolution of a landslide dam from impoundment through breaching, and stabilization.

In our experiment, the low-frequency band component (0–1.5 Hz) was related directly to the destabilization and failure of the dam. The collapse of the dam during the destabilization and dam failure stage led to further expansion of the breaches and caused an even larger water outburst. The rise in the energy level of the low-frequency component (0–1.5 Hz) indicated the occurrence of large-scale continuous outburst flooding. Hence, the low-frequency component of the seismic signal can be used to indicate the breaching of a landslide dam.

In addition to geologic factors that destabilize rocks in the vicinity of landslide dams, the deformation and subsidence of such dams, as well as erosion by the water flow, result in the occurrence of rockslides, which can be detected by the intermediate-frequency component (1.5–10 Hz). Rockslides can occur during the dam outburst or during the destabilizing and deformation period before failure. Therefore, the intermediate-frequency component could be used to evaluate the stability of the landslide dams before failure.

Based on the energy levels of the high-frequency component (10–45 Hz), the movement of the sediment in the areas near the dam breaches could be determined. The movement of the sediment can be used as an indicator of the scale of breaches of landslide dams.

The results of this study can be used as a reference for developing an early-warning system for landslide dam failure by monitoring and analyzing broadband seismic signals. According to the analysis presented above, we can summarize the energy of the seismic signal generated during a

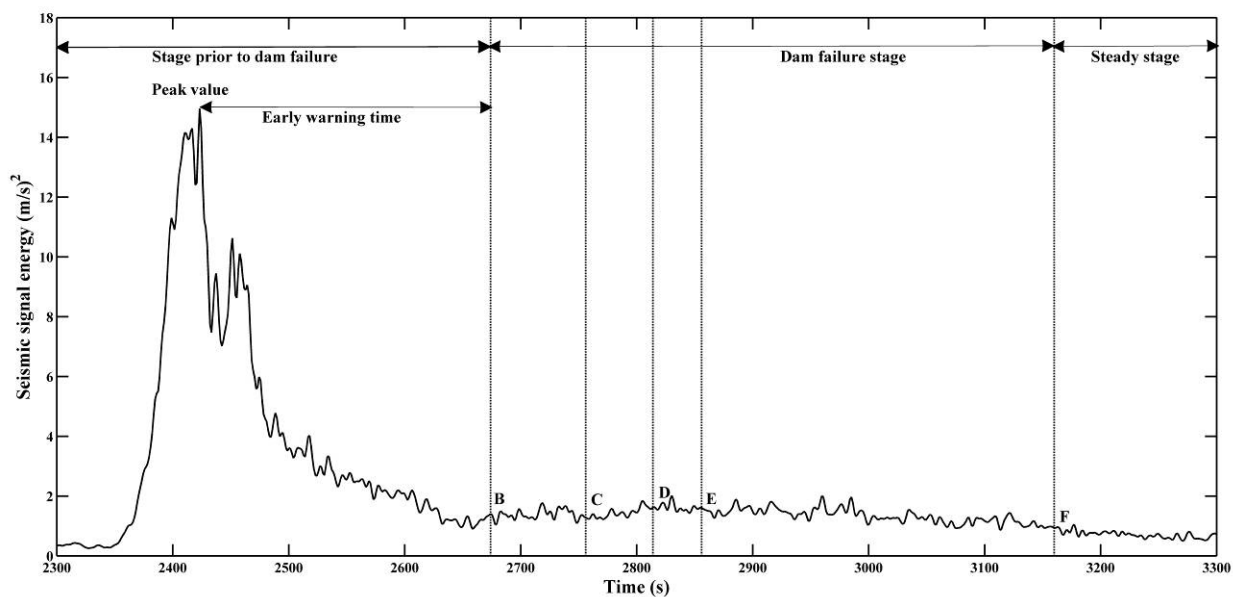


**Figure 14** Variation of the energy of the seismic signal with time in the landslide dam failure experiment.

landslide dam failure event (Figure 14), which can be used to determine the condition of the landslide dam, i.e., its stability. In section 4.3.2, we saw that the energy of the signal first increases and then decreases during the stage leading to dam failure. The energy peak appeared at 2423 s, and the dam burst at 2674 s, which gives 251 s of early warning time. Therefore, in future work, if the detected energy peak has passed and is declining, we can send out an early warning message of dam failure. This can be combined with monitoring and analysis of the low-frequency, intermediate-frequency, and high-frequency bands of the signal to evaluate the condition of the landslide dam. In practice hazards prevention, we can use the seismograph network to monitor the seismic signals to determine the approximate location and occur time of the landslide dam quickly. After locating the approximate position of the landslide dam, we should install the seismograph downstream of the landslide dam or near the landslide dam for signal monitoring.

In this study, we present a detailed analysis of the signal characteristics and causes during the landslide dam failure in a field-scale experiment. The landslide dam burst was due to overtopping. We propose a method of monitoring and early warning for overtopping-mode dam failures. Different dam failure modes would influence the signal. High frequency energy of overtopping mode was higher than the piping and slope failure,

meanwhile the clockwise effect was more obvious. So the characteristics of the seismic signal were applied only to the overtopping mode. We also carried out a qualitative and semi-quantitative analysis of the experimental process by signal analysis but did not perform a comprehensive quantitative analysis. However, we identified the mechanism that led to the changes in seismic signal from the perspective of the microscopic particles. Understanding of this mechanism is necessary for future quantitative analysis of the seismic signal. In future studies, a more detailed mathematical model of the relationship between the seismic signal and the dam failure process should be developed using more detailed measurement method and experimental design to further our understanding of the prevention and control of landslide dam disasters. Quantitative results of the dam failure process can be obtained by more experiments and prototype observation cases. We would consider more situations on piping and slope failure mode in the future. Finally, the early warning methods of different dam failure modes should be investigated.

## 5 Conclusions

In this study, the characteristics of the seismic signal during the landslide dam failure process were investigated using seismic signals and video

footage recorded during the simulated dam failure, as well as hydrodynamic parameters and soil mechanical parameters of the dam. Based on the results of the experiment, we conclude the following.

(1) We obtained the time–frequency characteristics of the seismic signal generated during the landslide dam failure; the signal consisted of three components: 0–1.5, 1.5–10, and 10–45 Hz. The energy generated in this experiment was mainly concentrated in the 10–45 Hz frequency band. In the intermediate-frequency-band, three short-term energy bands were identified, at 2682 s, 2982 s, and 3084 s. The low-frequency energy of the signal peaked in the middle of the time intervals 2708–2722 s, 2804–2851 s, and 2877–2947 s.

(2) The energy of the signal leading up to the dam’s failure varied significantly, i.e., a trend of initial increase followed by a decrease. The frequency width first widened and then narrowed. The PSDs initially increased and then decreased with water level variations. During the dam failure stage, the PSD in the high-frequency band (10–45 Hz) increased as the water level rose and decreased as the water level fell, showing clear rising and falling limbs, resulting in significant clockwise hysteresis.

(3) Analysis of the seismic and video records indicated that each frequency band of the seismic signal reflected different aspects of the dam failure process. The low-frequency component corresponds to the soil collapse of the dam, the intermediate-frequency component corresponds to rockslide, and the high-frequency component reflects the water-induced movement of the sediment.

(4) The variations in the energy and frequency

of the seismic signal before the dam failure reflected a dynamic process of inflow and return flow behind the upstream dam. The frequency width reflected the variation in water velocity, and the signal energy reflected the sediment transport capacity of the water. During the dam failure stage, the variation of the rising and falling limb of the water flow was the fundamental reason for the formation of the clockwise hysteresis.

## Acknowledgments

The Institute of Mountain Hazards and Environment of Chinese Academy of Sciences thank the Department of Soil and Water Conservation of National Chung Hsing University and the NCHU research group lead by Prof. Suchin CHEN for providing the opportunity to participate in such excellent field scale landslide dam failure experiment, and appreciate Prof. Suchin CHEN for sharing the experimental data. This study was financially supported by the External Cooperation Program of Bureau of International Co-operation, Chinese Academy of Sciences (131551KYBS20130003), the Risk Evaluation and Mitigation Technology of Barrier Lake Project of China Communications Construction Company Limited(2013318Jo1100), the Key Technologies R&D Program of Sichuan Province in China (2014SZ0163), the Special Program for International S & T Cooperation projects of China (Grant No. 2012DFA20980), and National Natural Science Foundation of China (Grant No.51479179). We thank Professor LI Yong and Dr. GUO Xiaojun from the Institute of Mountain Hazards and Environment, Chinese of Chinese of Sciences for the revision and suggestions on this paper.

## References

- Burtin A, Bollinger L, Cattin R, et al. (2009) Spatiotemporal sequence of Himalayan debris flow from analysis of high - frequency seismic noise. *Journal of Geophysical Research: Earth Surface* 114(F4). DOI: [10.1029/2008JF001198](https://doi.org/10.1029/2008JF001198)
- Burtin A, Bollinger L, Vergne J, et al. (2008) Spectral analysis of seismic noise induced by rivers: A new tool to monitor spatiotemporal changes in stream hydrodynamics. *Journal of Geophysical Research: Solid Earth* 113(B5). DOI: [10.1029/2007JB005034](https://doi.org/10.1029/2007JB005034)
- Chao WA, Wu YM, Zhao L, et al. (2015) Seismologically determined bedload flux during the typhoon season. *Scientific Reports* 5: 8261. DOI: [10.1038/srep08261](https://doi.org/10.1038/srep08261)
- Chen CH, Chao WA, Wu YM, et al. (2013) A seismological study of earthquakes using a real-time broad-band seismic network. *Geophysical Journal International* 194: 885-898. DOI: [10.1093/gji/ggt121](https://doi.org/10.1093/gji/ggt121)
- Chen S, Lin T and Chen C (2015) Modeling of natural dam failure modes and downstream riverbed morphological changes with different dam materials in a flume test. *Engineering Geology* 188: 148-158. DOI: [10.1016/j.enggeo.](https://doi.org/10.1016/j.enggeo.)



2015.01.016

- Costa JE, Schuster RL (1988) The formation and failure of natural dams. *Geological Society of America Bulletin* 100(7): 1054-1068. DOI: [10.1130/0016-7606\(1988\)100<1054-1068>2-B](https://doi.org/10.1130/0016-7606(1988)100<1054-1068>2-B)
- Cui P, Zhou GGD, Zhu XH, et al. (2013) Scale amplification of natural debris flows caused by cascading landslide dam failures. *Geomorphology* 182: 173-189. DOI: [10.1016/j.geomorph.2012.11.009](https://doi.org/10.1016/j.geomorph.2012.11.009)
- Cui P, Zhu Y, Han Y, et al. (2009) The 12 May Wenchuan earthquake-induced landslide lakes: distribution and preliminary risk evaluation. *Landslides* 6: 209-223. DOI: [10.1007/s10346-009-0160-9](https://doi.org/10.1007/s10346-009-0160-9)
- Dammeier F, Moore JR, Haslinger F, et al. (2011) Characterization of alpine rockslides using statistical analysis of seismic signals. *Journal of Geophysical Research: Earth Surface* 116(F4). DOI: [10.1029/2011JF002037](https://doi.org/10.1029/2011JF002037)
- Deparis J, Jongmans D, Cotton F, et al. (2008) Analysis of rock-fall and rock-fall avalanche seismograms in the French Alps. *Bulletin of the Seismological Society of America* 98: 1781-1796. DOI: [10.1785/0120070082](https://doi.org/10.1785/0120070082)
- Dietrich WE, Kirchner JW, Ikeda H, et al. (1989) Sediment supply and the development of the coarse surface layer in gravel-bedded rivers. *Nature* 340: 215-217. DOI: [10.1038/340215a0](https://doi.org/10.1038/340215a0)
- Feng Z (2011) The seismic signatures of the 2009 Shiaolin landslide in Taiwan. *Natural Hazards and Earth System Science* 11: 1559-1569. DOI: [10.5194/nhess-11-1559-2011](https://doi.org/10.5194/nhess-11-1559-2011)
- Feng Z (2012) The seismic signatures of the surge wave from the 2009 Xiaolin landslide - dam breach in Taiwan. *Hydrological Processes* 26: 1342-1351. DOI: [10.1002/hyp.8239](https://doi.org/10.1002/hyp.8239)
- Hanson GJ, Robinson KM, Cook KR (2001). Prediction of headcut migration using a deterministic approach. *Transactions of the ASAE* 44(3): 525. DOI: [10.13031/2013.6112](https://doi.org/10.13031/2013.6112)
- Hanson GJ, Cook KR, Simon A (1999). Determining erosion resistance of cohesive materials. In *Proc. ASCE Intl. Water Resources Eng. Conf.* Hsu L, Finnegan NJ and Brodsky EE (2011) A seismic signature of river bedload transport during storm events. *Geophysical Research Letters* 38(13). DOI: [10.1029/2011GL047759](https://doi.org/10.1029/2011GL047759)
- Huang CJ, Yeh CH, Chen CY, et al. (2008) Ground vibrations and airborne sounds generated by motion of rock in a river bed. *Natural Hazards and Earth System Science* 8: 1139-1147. DOI: [10.5194/nhess-8-1139-2008](https://doi.org/10.5194/nhess-8-1139-2008)
- Huang CJ, Yin HY, Chen CY, et al. (2007) Ground seismics produced by rock motions and debris flows. *Journal of Geophysical Research: Earth Surface* 112(F2). DOI: [10.1029/2005JF000437](https://doi.org/10.1029/2005JF000437)
- Humphries R, Venditti JG, Sklar LS, et al. (2012) Experimental evidence for the effect of hydrographs on sediment pulse dynamics in gravel-bedded rivers. *Water Resources Research* 48(1). DOI: [10.1029/2011WR010419](https://doi.org/10.1029/2011WR010419)
- Martin RL, Jerolmack DJ (2013) Origin of hysteresis in bed form response to unsteady flows. *Water Resources Research* 49: 1314-1333. DOI: [10.1002/wrcr.20093](https://doi.org/10.1002/wrcr.20093)
- Nanson GC (1974) Bedload and suspended-load transport in a small, steep, mountain stream. *American Journal of Science* 274: 471-486. DOI: [10.2475/ajs.274-5-471](https://doi.org/10.2475/ajs.274-5-471)
- Reid I, Frostick LE and Layman JT (1985) The incidence and nature of bedload transport during flood flows in coarse-grained alluvial channels. *Earth Surface Processes and Landforms* 10: 33-44. DOI: [10.1002/esp.3290100107](https://doi.org/10.1002/esp.3290100107)
- Roth DL, Finnegan NJ, Brodsky EE, et al. (2014) Migration of a coarse fluvial sediment pulse detected by hysteresis in bedload generated seismic waves. *Earth and Planetary Science Letters* 404: 144-153. DOI: [10.1016/j.epsl.2014.07.019](https://doi.org/10.1016/j.epsl.2014.07.019)
- Sassa K, Fukuoka H, Wang F, et al. (2005) Dynamic properties of earthquake-induced large-scale rapid landslides within past landslide masses. *Landslides* 2: 125-134. DOI: [10.1007/s10346-005-0055-3](https://doi.org/10.1007/s10346-005-0055-3)
- Schmandt B, Aster R, Scherler D, et al. (2013) Multiple fluvial processes detected by riverside seismic and infrasound monitoring of a controlled flood in Grand Canyon. *Geophysical Research Letters* 40: 1-6. DOI: [10.1002/grl.50953](https://doi.org/10.1002/grl.50953)
- Schuster RL (2006) Risk-reduction measures for landslide dams. *Italian Journal of Engineering Geology and Environment (Special Issue)* 1: 9-13. DOI: [10.4408/IJEGE.2006-01.S-01](https://doi.org/10.4408/IJEGE.2006-01.S-01)
- Tsai VC, Minchew B, Lamb MP, et al. (2012) A physical model for seismic noise generation from sediment transport in rivers. *Geophysical Research Letters* 39(2). DOI: [10.1029/2011GL050255](https://doi.org/10.1029/2011GL050255)
- Yamada M, Kumagai H, Matsushi Y, et al. (2013) Dynamic landslide processes revealed by broadband seismic records. *Geophysical Research Letters* 40: 2998-3002. DOI: [10.1002/grl.50437](https://doi.org/10.1002/grl.50437)
- Yan Y, Cui P, Guo XJ, et al. (2016) Trace projection transformation: A new method for measurement of debris flow surface velocity fields. *Frontiers of Earth Science* 1-11. DOI: [10.1007/s11707-016-0576-1](https://doi.org/10.1007/s11707-016-0576-1)